RSC Advances

ROYAL SOCIETY OF CHEMISTRY

www.rsc.org/advances

CO methanation over a macro-mesoporous Al_2O_3 supported Ni catalyst in a fluidized bed reactor

Jun Li, Li Zhou, Qingshan Zhu*, Hongzhong Li

State Key Laboratory of Multiphase Complex System, Institute of Process Engineering,

Chinese Academy of Sciences, Beijing 100190, P. R. China

Abstract

The synthesis and characterization of highly active and stable Ni nanoparticles supported on macro-mesoporous Al_2O_3 as a CO methanation catalyst for the production of synthetic natural gas are reported. The macro-mesoporous Ni-Al_2O_3 catalyst (MNC) is synthesized by combination of sol–gel and supercritical drying method. The MNC showed much higher activity and higher thermal stability of methanation than the catalyst via conventional wet impregnation method, especially under harsh conditions of higher temperatures and higher GHSV (90000 h^{-1}). The enhancement in activity of the synthesized MNC catalyst is attributed to the high stable and smaller Ni nanoparticles that embedded on the macro-mesoporous structure. The MNC also showed higher rate constant and lower diffusion activation energy, which should be attributed to the macro-mesoporous structure that facilitated the diffusion of products gas and then enhanced the reaction heat removal from the catalyst surface. Thus, lead to a higher resistance to Ni sintering and carbon deposition.

Keywords：Methanation; Nickel catalyst; Synthetic natural gas; Macro-mesoporous; Fluidized bed

* Corresponding Author's E-mail: qszhu@ipe.ac.cn (Q.S. Zhu)

1. Introduction

By virtue of high calorific value, smoke and slag free combustion properties, the natural gas is a highly efficient and clean fossil fuel.[1] The increased in demand for natural gas has lead one to pursue various routes to produce synthetic natural gas (SNG). Among the several routes of coal conversion, production of SNG via gasification of coal and the subsequent methanation of the synthetic gas (syngas) is an energy efficient process.[2-7] The methanation ($CO+3H_2 \rightarrow CH_4+H_2O$) of the syngas obtained by coal gasification is a key process during this transformation. The methanation reaction is a highly exothermic reaction accompanied by a large decrease in mole number.[8,9] The heat removal of methanation reaction has been a major concern of the industrial methanation process for avoiding deactivation of catalysts due to sintering of metal particles, carbon deposition and sulphur poisoning induced by higher temperature sites.[2] Thermodynamically, this reaction is favored at low temperature and high pressure but it is favored at high temperatures in kinetically, as well as in the views of optimizing utilization of heat values.[10] However, it is challenges to maintain good thermal stability and avoid deactivation of catalysts due to sintering of metal particles and carbon deposition at high temperatures.

Fluidized bed reactors have the advantages in preventing the carbon deposition and sintering of Ni catalysts due to almost isothermal conditions in the reactor, superior transfer and hydrodynamic characteristics. Fluidized bed reactors have been developed for production of SNG from coal or biomass, including the multiple-feed fluidized bed reactor,[11] the Bi-Gas project,[12] the Comflux process,[13] and the PSI fluidized bed methanation process.[14] The inevitably encountered axial gas and solids back-mixing and severe attrition in the fluidized

bed reactor play a negative role in the overall reactor performance.[8] From the perspective of the matching of catalyst and reactor, enhancing the diffusion of products gases and heat removal for based on catalyst structure designation would be feasible for improving the catalytic performance and thermal stability.

Nano-sized catalysts exhibiting unique morphological and physicochemical properties play a key role in heterogeneous catalysts.[15] Over the past decades, various metal nanoparticles have been employed to CO methanation reaction, such as Ni, Ru, Rh, Co, Fe, and Mo methanation catalysts.[16-21] Among the above active metal, catalysts based on Ni are frequently used for industrial applications, such as selective CO methanation to remove trance CO from H_2-rich feed gases for fuel cells, due to its relatively active and low cost.[22] However, when they are used for SNG production with large concentration of CO in the feed gases, the Ni catalysts tend to aggregate into large particles and prone to forming carbon deposition, which induce a rapid deactivation of the catalysts.[23] Thus, addition of small amount of second metal,[24,25] core-shell or hollow structure,[26,27] or meso/nanoporous particles[28,29] have to be introduced to improve the resistant to carbon deposition and to separate the metal nanoparticles from each other to prevent sintering. In addition, process intensification derived from the fluidized bed,[30] magnetic fields[31] and plasma assistant[32] have been explored to inhibit the sintering of metal nanoparticles and carbon deposition of catalysts. Recently, several chemical approaches that rely on the formation of alloy[33] or substrate effects[34] have also been developed to stabilize metal nanoparticles.

Up to now, most of the aforementioned catalysts were developed for the fixed bed reactor and focus on the size and dispersion of metal species, metal-support interaction and the

surface structures. However, the enhancement for the diffusion of products gases and heat removal based on the particle structure designation for methanation in the fluidized bed reactor are not reported in the literatures. In the present work, we aim to enhance the diffusion of products gases and heat removal for improving the catalytic performance and thermal stability based on catalyst structure designation as well as the perspective of the matching of catalyst and fluidized bed reactor. The macro-mesoporous Ni/Al_2O_3 catalyst is synthesized via a sol–gel method combined with a supercritical drying treatment for formation of highly dispersed Ni crystals embedded on macro-mesoporous Al_2O_3 nanoparticles. The prepared catalyst large surface area, highly dispersed Ni nanoparticles and a lot of macro-mesoporous structures. The catalytic performances of the macro-mesoporous catalyst for CO methanation were compared with a conventional Ni-based catalyst in a micro-fluidized bed reactor.

2. Experimental

2.1 Catalyst preparation

The macro-mesoporous $Ni\text{-}Al_2O_3$ catalyst (MNC) was synthesized by using a sol–gel method combined with a supercritical drying treatment according to the following procedure.[31] Firstly, a 2.5 wt% $NH_3{\cdot}H_2O$ solution was added dropwise to a 0.18mol/L Al^{3+} solution with continuously and vigorously stirring at room temperature until the pH value reached 7.5 to form a hydrogel. Subsequently, the $Ni(NO_3)_2$ solution with 0.1mol/L Ni^{2+} was added dropwise to the $Al(OH)_3$ hydrogel, followed by adjusting the pH value to 9.0 with $NH_3{\cdot}H_2O$ solution. Next, the as-prepared hydrogel was aged at room temperature for 2 h. After being thoroughly washed with distilled water and absolute ethanol for several times, the as-prepared ethanol-gel was then treated in the supercritical condition of ethanol (260 ^{o}C and

8.0 MPa) for 1 h. After releasing ethanol vapor at 260 ^{o}C, the resultant powders were cooled down to room temperature in a continuous nitrogen flow. Finally, the powders were calcined at 400-600 ^{o}C for 4 h in air to form the Ni aerogel catalyst. The Ni catalyst was designed to have an active metal loading of 40 wt% Ni after reduction.

The impregnation Ni/Al_2O_3 catalyst (denoted as INC) was prepared by the conventional impregnation method. The catalyst support used was a commercial Al_2O_3 with particle sizes of 70-90 μm, bulk density of 660 kg/m^3. Firstly, $Ni(NO_3)_2{\cdot}6H_2O$ was dissolved in distilled water, followed by the addition of Al_2O_3 particles. The slurry was stirred at room temperature for 8 h, and then dried at 120 ^{o}C for 4 h. The solid sample was afterwards calcined at 400 ^{o}C in air for 4 h. The content of NiO in the catalyst prepared was 40 wt%. Detailed preparation method of the Ni catalyst was shown in the ref. 30.

2.2 Catalyst characterization

The BET surface area of the catalysts was analyzed by the N_2 adsorption method at –196 ^{o}C in an adsorption instrument (Autosorb-1, Quantachrome, USA). The model used to calculate the pore size distribution is BJH method desorption pore size distribution.[35] The phase structure of the spent and fresh catalysts was characterized by using X-ray diffractometer (XRD, X'Pert MPD Pro, Panalytical, Netherlands) with Cu Kα radiation (λ=1.5408 Å) at 40 kV and 40 mA. The powders morphology of the catalysts was analyzed by field-emission scanning electron microscopy (FESEM, JSM-7001F, JEOL, Japan). The microstructure of the catalysts was analyzed by transmission electron microscopy (TEM, JEM-2100, UHR). The sample was dispersed in ethanol in an ultrasonic bath carefully and then deposited on copper mesh. The high angle annular dark field scanning transmission

electron microscope (HAADF-STEM) was obtained on A FEI Tecnai G2 F20 U-TWIN high-resolution transmission electron microscope (TEM) operated at 200 kV.

Temperature programmed reduction of hydrogen (H_2-TPR) was performed on a chemisorption apparatus (ChemBet 3000, Quantachrom, USA), which provide important information about the reduction difficult degree of Ni species and the interaction with the supports. The sample (15 mg) was loaded in a U-type quartz tube of 5mm diameter. The sample was pretreated with Ar (99.99%) flow at 200 °C for 60 min, followed by cooling it to room temperature. Then the sample was heated to 900 °C at a constant heating rate of 10 °C/min using a flow of H_2/Ar mixture (5%H_2, vol%) under a flow rate of 100 mL/min. The signal of hydrogen consumption was detected by a thermal conduction detector (TCD).

Hydrogen chemisorption was also performed on the chemisorption apparatus (ChemBet 3000, Quantachrom, USA). The sample was first pre-reduced with purified H_2 at 600 °C for 2 h using a heating rate of 10 °C/min. The sample was purged with helium at this temperature for 1h and it was then cooled to room temperature for the chemisorption measurement.

The thermogravimetric and differential thermal analyzer, TG/DTA6300 model, was used to analyze the carbon deposition of the spent catalyst, operated in a temperature range from room temperature to 900 ^{o}C at a heating rate of 10^{o}C/min.

2.3 Catalytic reaction

The methanation performances of the catalysts were performed in a micro-quartz fluidized reactor analyzer system,[36] including a feed gas system, a micro-quartz fluidized reactor (i.d. of 16 mm) collocated with a heat furnace and a GC analyzer. The reactions were tested over a temperature range of 200-500 ^{o}C. The gas hourly space velocity (GHSV, h^{-1}) was selected to

be 30,000 h^{-1} under atmospheric pressure. The gas velocity (u) was 0.02 m/s under standard conditions (u/u_{mf}=4).

The amounts of MNC and INC catalysts were fixed to be 0.2 g. To keep the same GHSV value, the INC catalyst was mixed with Al_2O_3 particles with settled bed height of 12 mm. The feed gas consisted of CO, H_2, N_2 with a molar ratio of 1:3:1, where N_2 was added as the fluidized gas and also as an internal standard gas for GC analysis. In the experiment, the Ni catalyst was pre-reduced in pure H_2 with flow rate of 100 mL/min at 600 ^oC for 4 h. Then, the feed gas was supplied up-flow through a porous quartz sintered distributor at the bottom of the reactor to allow fluidization of the catalyst particles. The outlet gas stream was cooled by using an ice trap. To determine the composition of outlet gas products, the gas products (H_2, N_2, CH_4, CO_2 and CO) were collected after half an hour of steady-state operation for each temperature and analyzed by GC (3000 Micro GC, Inficon). The calculation formulas for CO conversion, CH_4 selectivity and yield were calculated as follows:

$$\text{CO conversion: } X_{CO}(\%) = \frac{V_{CO,in} - V_{CO,out}}{V_{CO,in}} \times 100 \quad (1)$$

$$\text{CH}_4\text{ selectivity: } S_{CH_4}(\%) = \frac{V_{CH_4,out}}{V_{CO,in} - V_{CO,out}} \times 100 \quad (2)$$

$$\text{CH}_4\text{ yield: } Y_{CH_4}(\%) = \frac{V_{CH_4,out}}{V_{CO,in}} \times 100 \quad (3)$$

where X is the conversion, S is the selectivity, Y is the yield, $V_{i,in}$ (mL/min) and $V_{i,out}$ (mL/min) are the inlet and outlet volumetric flow rate of species i (i = CO, CO_2, H_2, and CH_4), respectively.

The effect of GHSV on the catalytic reaction of the MNC and INC catalysts were carried out at 400 ^oC in the GHSV range of 7500-90000 h^{-1}. The stability tests of the MNC and INC

catalyst were carried out at 350 ^{o}C with GHSV of 30000 h^{-1}. A thermocouple was put into the central section of the catalyst bed to measure the reaction temperature with average error less than 5 %. All the tests were duplicated to ensure accuracy, and the carbon balance across the reactor was within ±2%.

2.4 Kinetics methodology

In this study, additional assumption was made that the apparent reaction is the first-order rate constants for CO dissociation on the surface. A parabolic law was used to describe the CO methanation that occurs in the fluidized bed of this study, it can be expressed as[37]:

$$\ln(\frac{1}{1-x}) = kt \quad (4)$$

Where x is the conversion of CO, k is the reaction rate constant and t is the reaction time in second.

The rate of the CH_4 formation can be described by the following equation[38]:

$$r_{CH_4} = Ae^{-E/RT} P_{CO}^{a} P_{H_2}^{b} \quad (5)$$

Where r_{CH_4} is the rate of CH_4 formation, A is the pre-exponential factor, E is the apparent activation energy, P_i presents gas partial pressure of species i (i=CO, H_2), a and b are the exponents of the partial pressures of hydrogen and monoxide, respectively.

From equation (5) we can obtain

$$\ln r_{CH_4} = -E/RT + C \quad (6)$$

The yield of CH_4 and CH_4 formation rate are in direct ratio

$$r_{CH_4} = mY_{CH_4} \quad (7)$$

where R is mole gas constant (8.314 J /(mole·K)), T is absolute temperature (K), C is some certain value, and m is the direct ratio.

The apparent activation energy (E) can be determined from the slope of the plot of $\ln r_{CH_4}$ against 1/*T*.

3. Results and discussion

3.1 Catalyst characterization

Figure 1 shows the TPR profiles for the MNC and INC catalysts. Two major reduction peaks at 230 °C and 680°C were observed for the INC catalyst (**Figure 1d**). The first peak could be attributed to the reduction of the bulk NiO species, which had weak interaction with the support.[39,40] The second peak at 680 ^{o}C was due to the reduction of a small NiO species strongly interacting with the support.[41,42] For the MNC catalysts calcined at 400-600 ^{o}C, there were more than one reduction peak in the temperature range of 200-800°C. With the calcinations temperature increased, the reduction peaks moved to higher temperatures (**Figure 1a-c**), which indicated a stronger interaction with the support. Compared to INC, the MNC calcined at 600 ^{o}C showed less bulk NiO species, but more small NiO species that had a strong interaction with the support, which is hard to be reduced. However, the MNC calcined at 400 ^{o}C and 500 ^{o}C showed NiO species between bulk NiO species and the small NiO species, which is conducive to suppressing the formation of deposited carbon.

The isothermal adsorption-desorption curves of the MNC and INC catalysts are shown in **Figure 2A**. The MNC catalysts showed a clear hysteretic behavior in the N_2 physisorption curves that attributed to the mesopores (range 2-50 nm). All of the MNC catalysts showed a broad desorption curves that consist of mesopores and macropores (**Figure 2B**). The broad desorption curves that above 50 nm might be attributed to the aggregation of the smaller particles. These results could be confirmed in the SEM images of the MNC catalyst (**Figure**

3a). Nevertheless, a relatively smaller desorption peak with average pore size of 12.1 nm was observed for the INC catalyst. Compared to the INC, the MNC exhibited much larger mesoporous than the INC, which would be highly desirable for high exothermic methanation reaction. High BET surface and enriched macropores are conducive to not only the dispersion of the nickel species but also the diffusion of the reactants and products, namely the mesopore frameworks can provide more accessible active sites for the reactants.[43]

Figure 3a (insert) and **3b** showed the well dispersed Ni nanoparticles embedded on mesoporous Al_2O_3 after calcined at 400 ^oC and further reduced at 600 ^oC. They had Al_2O_3 particle sizes of 23.3 nm and Ni crystalline sizes of 4.8 nm. As can be seen in **Figure 3c** and **3d**, the INC exhibited Al_2O_3 particle sizes of 60.0 nm and crystalline sizes of 10.8 nm. The obvious heterogeneous distribution of the Ni crystalline sizes was observed from **Figure 3d**.

The physicochemical properties of the MNC and INC catalysts are summarized to **Table 1**. As comparison with INC, the MNC showed extremely low bulk density, higher dispersed Ni nanoparticles and higher specific surface areas than that of the INC. This should be attributed to the differences of preparation method. In the sol–gel process, Ni species could be uniformly dispersed and reached to atomic or molecular level interaction with support. The skeleton of the original sol–gel was almost kept intact in the aerogel, as in the supercritical drying process, the influence of surface tension and capillary force on the gel skeleton can be neglected.[44] While in the case of the conventional preparation process, the dispersion of nickel species could block part of pores on support and resulted in the lower specific surface area. Thus, the MNC exhibited high specific surface areas, low bulk density, small Ni crystalline sizes, strong metal-support interaction and high Ni dispersion degrees, which make

them an ideal material for heterogeneous catalysis.

3.2 Catalytic activity

Comparison of methanation catalytic activity of the two Ni-based catalysts in the temperature range of 200-500 ^{o}C is shown in **Figure 4**. In the presence of INC catalyst, the conversion of CO was 75-95 % and the selectivity of CH_4 was 70-80 % in the temperature range of 200-500 ^{o}C. The selectivity and yield of CH_4 were much less than the thermodynamic equilibrium values under lower temperatures. When the reaction temperature was above 400 ^{o}C, the conversions of CO decreased rapidly and got far from the thermodynamic equilibrium values. This indicated that the INC was not active enough to convert the entire CO due to the diffusion limitation under high temperatures.[30] Compared to the INC, the selectivity and yield of CH_4 with MNC were increased 8-10 percentages, and the CO conversion was increased 3-5 percentages. These results should be attributed to the structure of the MNC catalyst. The abundant mesoporous facilitated the diffusion of products gas, which is particularly important for selectivity of CH_4. As compared to other macro-mesoporous and non-macro-mesoporous Ni-Al_2O_3 catalysts previous reported in the literatures,[11,45,46] the MNC also exhibited a slightly higher selectivity of CH_4, but obvious higher CO conversion. With the temperature increased, the inevitable decreases of CO conversion and selectivity of CH_4 were observed for the MNC catalyst due to the thermodynamic equilibrium limitation. As is mentioned above, the methanation reaction is favored at low temperature thermodynamically. However, in view of heat utilization, the methanation process at higher temperatures is a quite encouraging choice to achieve higher quality superheated steam.[10] However, the high temperatures will require high stability

catalyst for inhibiting Ni sintering and carbon formation. Moreover, at typical conditions, excellent heat transformation for catalyst and reactors is key factor for inhibiting Ni sintering and carbon formation at high temperatures.

The increase in temperature during the methanation reaction is shown in **Figure 5**. For INC catalyst, the temperature increased about 115 ^{o}C at the reaction temperature of 315 ^{o}C. When the reaction temperature was higher than 315 ^{o}C, the temperature rise decreased with increasing methanation reaction temperature. MNC shows a similar trend of temperature rise curve. However, MNC has a much lower temperature rise compared to INC. This indicated that MNC enhanced the heat transfer from the catalyst particle phase to the gas phase. The enhanced heat transfer property of MNC should be attributed to the macro-mesoporsous structure that enhanced gas-products diffusion efficiency.

Comparison the catalytic activity and thermal stability of the MNC and INC catalysts at 350 ^{o}C are illustrated in **Figure 6**. It shows that the conversion of CO, selectivity and yield of CH_4 over the MNC catalyst were much higher than those over the INC catalyst. For INC catalyst, the CO conversion, selectivity and the yield of CH_4 decreased from 99.0%, 78.7% and 77.6% to 96.2%, 72.2% and 69.5% respectively, indicating some deactivating of INC catalyst. However, for MNC catalyst, no obvious decrease in CO conversion, selectivity and the yield of CH_4 are observed. This suggested that the MNC catalyst would have better catalytic activity and thermal stability.

It is well known that the carbon deposition and sintering of the catalyst particles at high temperature deteriorate the activity of the catalyst during the CO methanation process.[47,48] **Figure 7** shows the XRD patterns of the fresh reduced catalysts and the spent catalysts after

methanation reaction test. The obvious diffraction peaks (2θ=44.5°, 51.7° and 76.2°) ascribed to Ni phases were observed in both fresh and spent catalysts. The fresh MNC (**Figure 7a**) exhibited much weaker and broader Ni XRD peaks than the fresh INC catalyst (**Figure 7c**), which indicated the Ni particle sizes of the MNC are much smaller than that of the INC. The Ni peaks of both spent MNC catalyst (**Figure 7b**) and spent INC catalyst (**Figure 7d**) showed slightly increased compared to their fresh catalysts respectively, suggesting a little increase in Ni crystalline size of spent catalysts. The Ni crystalline sizes of the fresh and spent MNC and INC catalysts were calculated from the Ni (111) diffraction peak using the Scherrer equation. The shape factor (K) used in the Scherrer equation was 0.94. As can be seen in **Table 2**, compared to the fresh catalyst, the Ni crystalline sizes of the spent INC catalyst increased to 15.3nm from 10.3nm, indicating a fast sintering of the Ni crystalline particles. However, the Ni crystalline sizes of the spent MNC catalyst showed little changes, only from 4.6nm to 5.1 nm compared the fresh catalyst. This was further corroborated with the STEM analysis. From the STEM images of Ni crystalline size of the fresh (**Figure 8a**) and spent MNC catalyst (**Figure 8b**), the Ni crystalline size shows no obvious change. In contrast, much sintering of Ni crystalline in the spent INC catalyst were observed (**Figure 8d**), as compared to the fresh INC catalyst (**Figure 8c**). This kind of sintering of Ni particles would undoubtedly bear the responsibility for the deactivation of the INC catalyst. Previous investigation revealed that the Ni particles growth rate is related to the particles size,[49] supports[50] and reaction temperatures.[51] It was shown that the rate of Ni sintering is lower for MNC catalysts than INC catalyst, which would be attributed to macro-mesoporsous structure that facilitated the reaction heat removal during the methanation process.

The TG-DTA analysis of the spent MNC catalyst after 50 h stability test is shown in **Figure 9a**. The mass loss below 252 ^{o}C is attributed to the moisture and the volatile species adsorbed on the catalyst. The mass gain from 252 ^{o}C to 291 ^{o}C is ascribed to the oxidation of the metallic nickel species.[52] The mass loss from 291 ^{o}C to 671 ^{o}C that belongs to the oxidation of carbon species on MNC is 0.05 mg, which accounting for 1.5 wt% of the total catalyst. The exothermic peak at 400^{o}C in the DTA curve is designated as the active carbon, which is responsible for the formation of SNG.[53] However, for the spent INC catalyst (**Figure 9b**), the exothermic peak at higher temperature of 680 ^{o}C in DTA curve is attributed to the inactive carbon which is responsible for the deactivation of the catalyst.[53] Correspondingly, the mass loss from 437 ^{o}C to 900 ^{o}C that ascribed to the inactive carbon is 0.461 mg, accounting for 3.9% of the total INC catalyst. Comparing the mass loss of carbon, the amount of carbon deposition on MNC was less than those on INC catalyst. Moreover, most of the carbon depositions on MNC are active carbon, while those on INC are mostly inactive carbon. This is reason why the MNC catalyst could maintain a high catalytic performance during the time on stream. This higher performance in preventing carbon deposition is probably attributed to the relatively smaller Ni crystalline size of MNC catalyst than that of the INC catalyst. On the other hand, the attrition of INC catalyst in the fluidized bed reactor may also be the reason for the decreased activity of INC catalyst.

3.3 Kinetics and catalytic activity energy

The kinetics of CO methanation over Ni-based catalysts have been studied intensively. It was generally believed that methanation proceeds via a COH_x intermediate.[14] Alstrup[54] proposed a microkinetic model with CH* + H* as the rate determing step, where the

coverages of CO, hydrogen, and carbon were significant. Sehested et al found that the kinetics of CO methanation reaction is well described by a first-order expression with CO dissociation at the nickel surface as the rate-determining step.[55]

Figure 10 showed the conversion of CO versus to reaction time, which were used for the fitting curves. The pseudo curves agrees well with the experimental data suggested that the parabolic law model gave a good agree to the kinetics data. The pseudo rate constant of MNC are nearly three times higher than the INC catalyst.

In order to better understand the effect of mesoporous structure on the catalytic activity of catalysts, the rate-determining step of CO methanation, kinetics and catalytic activity energy were also investigated. The curves of $\ln r_{CH_4}$ versus to $1/T$ are shown in **Figure 11**. The CH_4 formation rates (r_{CH_4}) are calculated from the yield of CH_4 in the temperatures range of 250-350 ^{o}C. It can be seen that the apparent activation energy of MNC and INC are 2.4 kJ/mol and 7.1 kJ/mol. The low apparent activity energy suggested a mass transfer controlling of CO methanation. Sehested et al also found the diffusion restrictions are most important at high activities and low CO concentrations due to the high conversions of CO in this cases.[55] This result indicated that the diffusion activation energy of MNC is less than that of INC. This would be attributed to the enhanced gas diffusion of the large mesoporous of MNC catalyst to the CO methanation. The enhanced diffusion improves the reactivity of CO methanation and leads to a higher rate constant. It is expected that the enhanced gas diffusion of the large mesoporous structures are favor for the heat removal from the surface of catalyst. Thus, lead to a higher resistance to Ni sintering and less carbon deposition. Generally speaking, there will be more errors about the K and E_a obtained by a micro-fluidized reactor than that by

micro-fixed reactor. And the value of CH_4 formation rates obtained from high yield of CH_4 also brings errors to the reaction activation energy. However, the fitting curves of **Figure 10** based on the E_a and K was coincident highly with the experimental data. The apparent reaction activation energy showed here was to illuminate the reactivity of CO methanation in the fluidized bed reactor.

4. Conclusions

In summary, the Ni-Al_2O_3 catalyst (MNC) synthesized by sol–gel combined with a supercritical drying treatment methods exhibited much higher selectivity and yield of CH_4 than the catalyst synthesized by conventional impregnation method (INC), especially under harshly conditions of higher temperatures and higher GHSV. The MNC also showed higher rate constant and lower diffusion activation energy. The enhancement in activity and thermal stability the MNC catalyst were attributed to extremely fine and high dispersion of Ni active species on macro-mesoporous Al_2O_3 that facilitated the diffusion of products gas and enhanced the reaction heat removal from the catalyst surface, which is particularly important for obtaining high resistance to Ni sintering and less carbon deposition.

Acknowledgements

We thank the financial support from the Training Program of the Major Research Plan of National Natural Science Foundation of China (No. 91334108), the National Instrumentation Grant Program (2011YQ12003908) and the China National Funds for Distinguished Young Scientists (21325628).

References

1 J. Kopyscinski, T.J. Schildhauer and S.M.A. Biollaz, *Fuel*, 2010**, 89**, 1763–1783.

2 Z.H. Liu, B.Z. Chu, X.L. Zhai, Y. Jin and Y. Cheng, *Fuel*, 2012, **95**, 599–605.

3 J. Liu, J. Yu, F.B. Su and G.W. Xu, *Catal. Sci. Technol.*, 2014, **4**, 472–481.

4 Y.J. Ding, W.J.Han, Q.H. Chai, S.H. Yang and W. Shen, Energy Policy, 2013, **55**, 445–453.

5 M. Sudiro and A. Bertucco, Natural Gas, 2010, **5**, 105–126.

6 J.M. Panek and J. Grasser, U.S. Department of Energy, 2006.

7 Z.Z. Liu, Ph.D thesis, University of California, 2014.

8 J. Kopyscinski, T. J. Schildhauer, and S.M.A. Biollaz, *Chem. Eng. Technol.*, 2009, **32**, 343–347.

9 O. Görke, P. Pfeifer and K. Schubert, *Catal. Today*, 2005, **110**, 132–139.

10 J.R. Rostrup-Nielsen, K. Pedersen and J. Sehested, *Appl. Catal., A*, 2007, **330**, 134–138.

11 M.D. Schlesinger, J.J. Demeter and M. Greyson, *Ind. Eng. Chem.* 1956, **48**, 68–70.

12 J.T.J. Cobb and R.C. Streeter, *Ind. Eng. Chem. Proc. Des. Dev.* 1979, **18**, 672–679.

13 W. Lommerzheim and C. Flockenhaus, In: Proceeding of tenth synthetic pipeline gas symposium, Chicago, American Gas Association, **1978**, P439–451.

14 J. Kopyscinski, T. J. Schildhauer and S.M.A. Biollaz, *Ind. Eng. Chem. Res.*, 2011, **50**, 2781–2790.

15 N. Li, J.J. Du, L.J. Xu, J.X. Xu and T.H. Chen, *Chem. Eng. J.*, 2014, **240**, 161–168.

16 J. Liu, W.L. Shen, D.M. Cui, J. Yu, F.B. Su and G.W. Xu, *Catal. Comm.*, 2013, **38**, 35–39.

17 F. Masini,, C.E. Strebel, D.N. McCarthy, A.U.F. Nierhoff, J. Kehres, E.M. Fiordaliso, J.H. Nielsena and I. Chorkendorff, *J. Catal.*, 2013, **308**, 282–290.

18 T. Szailer, É. Novák, A. Oszkó and A. Erdőhelyi, *Topics in Catalysis*, 2007, **46**, 79−86.

19 J.X. Liu, H.Y. Su and W.X. Li, *Catal. Today*, 2013, **215**, 36–42.

20 A. Govender, D.C. Ferre and J.W. Niemantsverdriet, *ChemPhysChem*, 2012, **13**, 1591−1596.

21 J. Chen, S.L. Li, Q. Xu and K. Tanaka, *Chem. Commun.*, 2002, **16**, 1722–1723.

22 J. Sehested, S. Dahl, J. Jacobsen and J. R. Rostrup-Nielsen, *J. Phys. Chem. B*, 2005, **109**, 2432–2438.

23 C. Bartholomew, *Catal. Rev. Sci. Eng.*, 1982, **24**, 67–112

24 Q. Liu, F.N. Gua, X.P. Lu, Y.J. Liu, H.F. Li, Z.Y. Zhong, G.W. Xu and F.B. Su, *Appl. Catal., A*, 2014,**488**,37–47.

25 C.K. Yuan, N. Yao, X.D. Wang, J.G. Wang, D.Y. Lv and X.N. Li, *Chem. Eng. J.*, 2015, **260**, 1–10.

26 Y.R. Li, G.X. Lu and J.T. Ma, *RSC Adv.*, 2014, **4**, 17420–17428.

27 H. Liu, J.L Qu, Y.F. Chen, J.Q. Li, F. Ye, J.Y. Lee and J. Yang, *J. Am. Chem. Soc.*, 2012, **134**, 11602−11610.

28 K. Tao, L. Shi, Q.X. Ma, D. Wang, C.Y. Zeng, C.L. Kong, M.B. Wu, L. Chen, S.H. Zhou, Y.B. Hu and N. Tsubaki, *Chem. Eng. J.*, 2013, **221**, 25–31.

29 M.A.A. Aziz, A.A. Jalil, S. Triwahyono and M.W.A. Saad, *Chem. Eng. J.*, 2015, **260**, 757–764。

30 J. Li, L. Zhou, P.C. Li, Q.S. Zhu, J.J. Gao, F.N. Gu and F.B. Su, *Chem. Eng. J.*, 2013, **219**, 183−189.

31 J. Li, L. Zhou, Q.S. Zhu and H.Z. Li, *Ind. Eng. Chem. Res.*, 2013, **52**, 6647–6654.

32 E. Jwa, S.B. Lee, H.W. Lee and Y.S. Mok, *Fuel Process. Technol.*, 2013, **108**, 89–93.

33 J.Y. Zhang, Z. Xin, X. Meng, Y.H. Lv and M. Tao, *Ind. Eng. Chem. Res.*, 2013, **52**, 14533−14544.

34 N. Ta, J.Y. Liu, S. Chenna, P. A. Crozier, Y. Li, A. Chen and W.J. Shen, *J. Am. Chem. Soc.*, 2012, **134**, 20585−20588.

35 J. Villarroel-Rocha, D. Barrera and K. Sapag, Microporous and Mesoporous Materials, 2014, **200**, 68–78

36 J. Yu, J.R. Yue, Z.E. Liu, L. Dong, G.W. Xu, J.H. Zhu, Z.K. Duan and L.X. Sun, *AIChE J.*, 2010, **56**, 2905−2912.

37 S.W. Churchill, B. Yu and Y. Kawaguchi, *Ind. Eng. Chem. Res.*, 2008, **47**, 5132–5145.

38 M.A. Vannice, *J. Catal.*, 1982, **74**, 199–202.

39 Q. Liu, J.J. Gao, M.J. Zhang, H.F. Li, F.N. Gu, G.W. Xu, Z.Y. Zhong and F.B. Su, *RSC Adv.*, 2014, **4**, 16094−16103.

40 V.M. Shinde and G. Madras, *AIChE J.*, 2014, **60**, 1027−1035.

41 J.M. Rynkowski, T. Paryjczak and M. Lenik, *Appl. Catal., A*, 1993, **106**, 73–82.

42 C.M. Jia, J.J. Gao, J. Li, F.N. Gu, G.W. Xua, Z.Y. Zhang and F.B. Su, *Catal. Sci. Technol.*, 2013, **3**, 490–499.

43 X.Z. Yang, Wendurima, G.J. Gao, Q.Q. Shi, X. Wang, J. Zhang, C.H. Han, J. Wang, H.L. Lu, J. Liu and M. Tong, *Int. J. Hydrogen Energy*, 2014, **39**, 3231−3242.

44 S. Hwang, J. Lee, U.G. Hong, J.G. Seo, J.C. Jung, D.J. Koh, H. Lim, C. Byun and I.K. Song, *J. Ind. Eng. Chem.*, 2010, **17**, 154−157.

45 X.Z. Yang, X. Wang, G.J. Gao, Wendurima, E.M. Liu, Q.Q. Shi, J.A. Zhang, C.H. Han, J. Wang, H.L. Lu, J. Liu and M. Tong, Int. J. Hydrogen Energy 2013, **38**, 13926–13937.

46 J.J. Gao, C.M. Jia, J. Lia, M.J. Zhang, F.N. Gua, G.W. Xu, Z.Y. Zhong and F.B. Su, Journal of Energy Chemistry, 2013, **22**, 919–927.

47 J.H. Kim, D.J. Suh, T.J. Park and K.L. Kim, *Appl. Catal., A*, 2000, **197**, 191–200.

48 T. Osaki, T. Horiuchi, T. Sugiyama, K. Suzuki and T. Mori, *Catal*, *Lett.*, 1998, **52**, 171–180.

49 Ø. Borg, S. Eri, E.A. Blekkan, S. Storsæter, H. Wigum, E. Rytter and A. Holmen, *J. Catal.*, 2007, **248**, 89–100.

50 J. Barrientos, M. Lualdi, M. Boutonnet and S. Järås, *Appl. Catal., A.*, 2014, **486**, 143–149.

51 J. Sehested, *Catal. Today*, 2006, **111**, 103−110.

52 L.A. Arkatova, *Catal. Today*, 2010, **157**, 170−176.

53 Y.G. Chen, K. Tomishige and K. Fujimoto, *Appl. Catal., A*, 1997, **161**, L11−L17.

54 I. Alstrup, *J. Catal.*, 1995, **151**, 216−225.

55 J. Sehested, S. Dahl, J. Jacobsen and J.R. Rostrup-Nielsen, *J. Phys. Chem. B*, 2005, **109**, 2432−2438.

Table 1 Physicochemical property of the MNC and INC catalyst

Catalysts	MNC	INC
Bulk density (kg/m^3)	80	660
BET[a] (m^2/g)	350	166
Average pore diameter (nm)	46.7	12.1
Ni dispersion[b] (%)	15.7	5.5

[a]Measure quantity of catalyst are about 0.1g

[b]Based on the H_2 chemisorption, assuming H_{ad}/Ni_s =1

Table 2 The Ni crystalline size and the amount of deposited carbon in spent catalyst samples

Catalysts	Ni crystalline size [a] (nm)	Deposited carbon (wt.%)
Fresh MNC	4.6	-
Fresh INC	10.3	-
MNC-50h	5.1	1.5
INC-50h	15.3	3.9

[a] Calculated from the (1 1 1) diffraction peak using the Scherrer equation

Figure Caption

Figure 1 H_2-TPR profiles of MNC after calcination at 400 ^oC (a), 500 ^oC (b), 600 ^oC (c) and INC after calcination at 400 ^oC (d) for 4 h

Figure 2 The isothermal adsorption-desorption curves (A) and the pore distribution (B) of MNC after calcination at 400 ^oC (a), 500 ^oC (b), 600 ^oC (c) and INC after calcination at 400 ^oC (d) for 4 h

Figure 3 SEM, TEM images and particle size distributions for MNC (a, b) and INC (c, d) after calcination at 400 ^oC and further reduced at 600 ^oC for 4h.

Figure 4 Catalytic activity of MNC and INC in the temperature range of 200-500 ^oC with GHSV of 30000 h^{-1}: CO conversion (a), CH_4 selectivity (b), (c) CH_4 yield.

Figure 5 The temperature rise during methanation reaction with MNC and INC catalysts.

Figure 6 Stability test of MNC and INC catalyst in a fluidized bed reactor at 350 ^oC. CO conversion (a), CH_4 selectivity (b), and (c) CH_4 yield

Figure 7 XRD patterns of the spent MNC (b) and INC (d) in comparison of the fresh MNC (a) and INC (c).

Figure 8 High-angle annular dark-field (HAADF)-STEM images of the fresh and spent MNC (a, b), and fresh and spent INC (c, d) after 50h reaction.

Figure 9 TG-DTA analysis of the spent MNC (a) and INC (b) catalyst after 50 h reaction

Figure 10 The conversion of CO versus to reaction time

Figure 11 The curve of $\ln \mathbf{r}_{CH_4}$ versus to 1/T

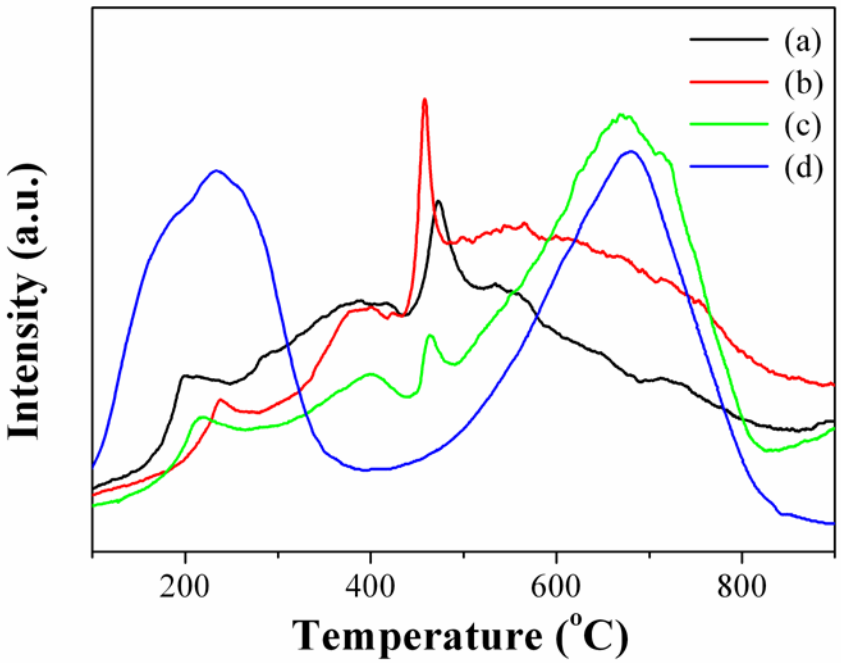

Figure 1

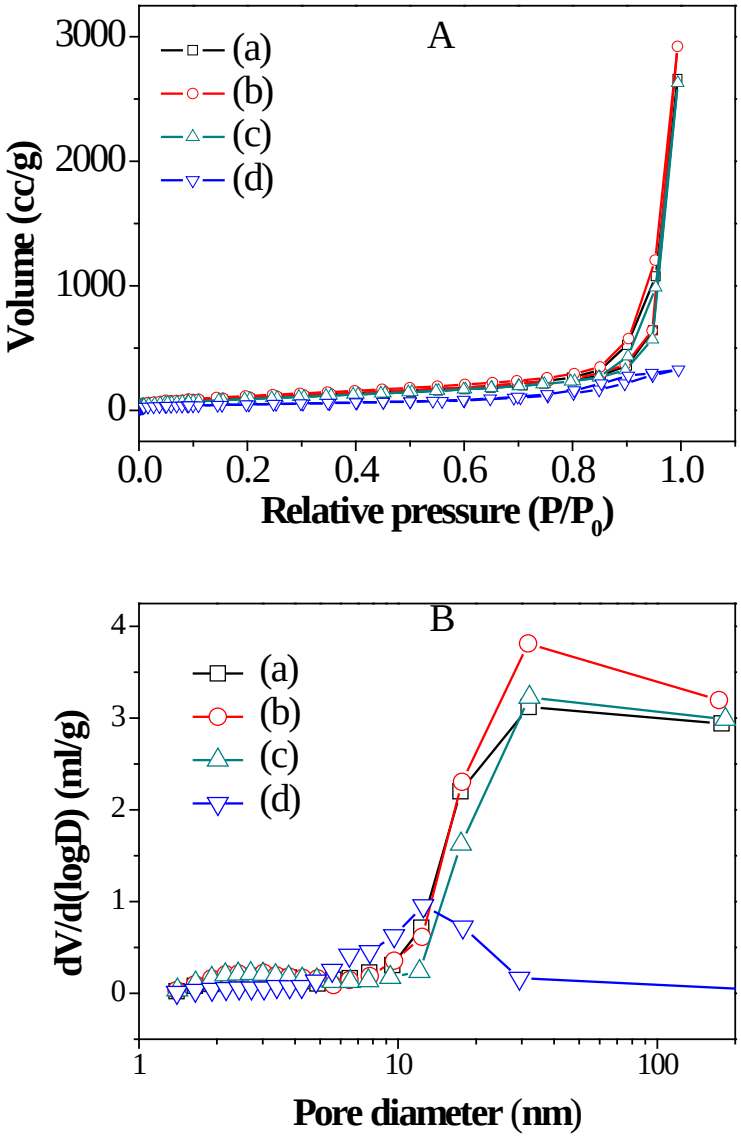

Figure 2

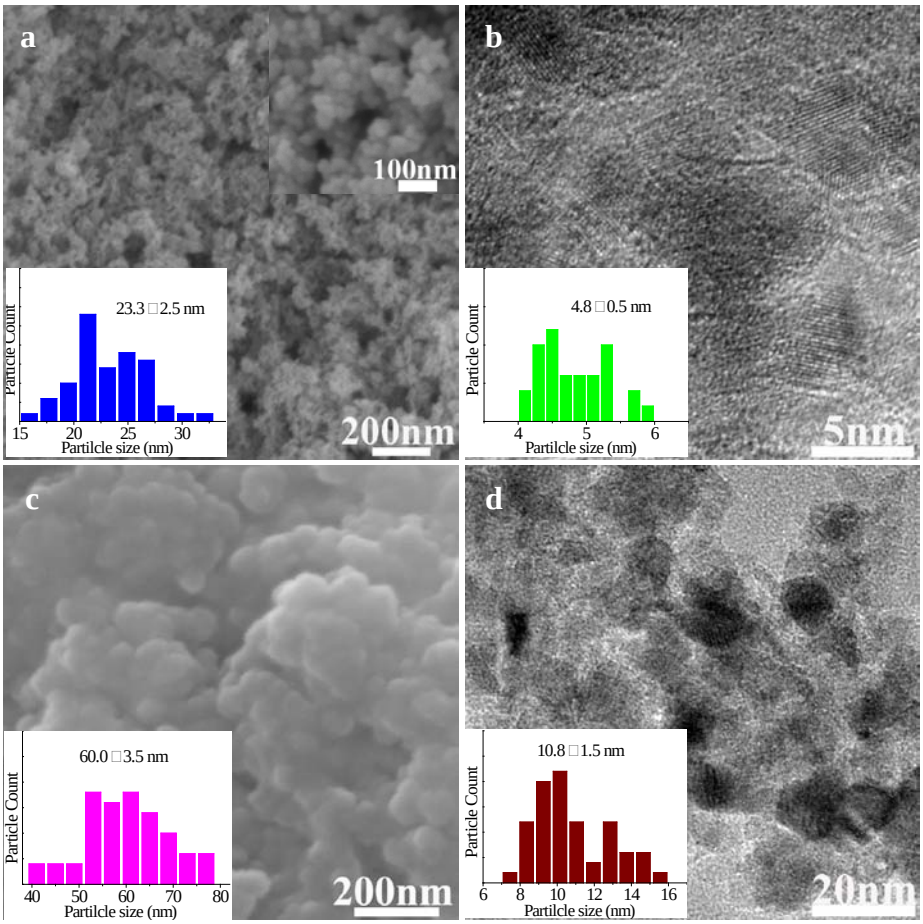

Figure 3

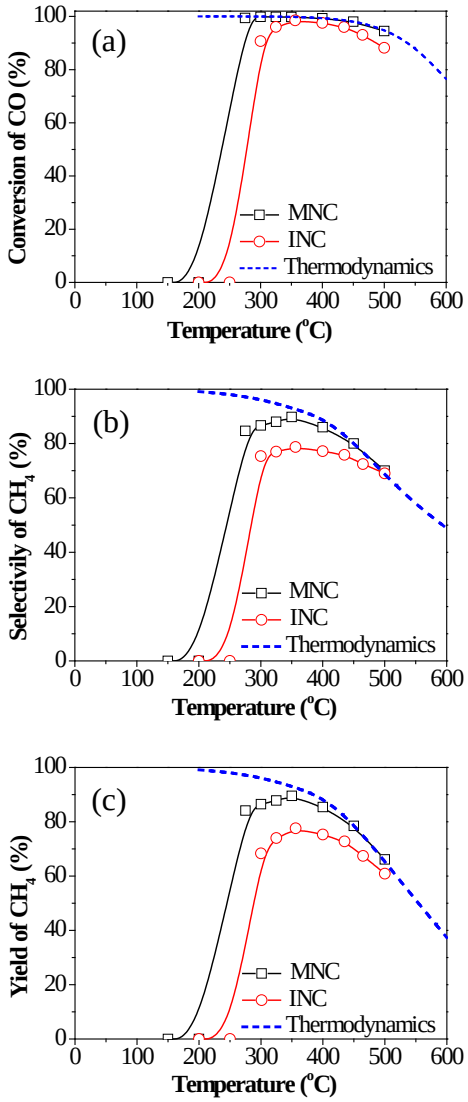

Figure 4

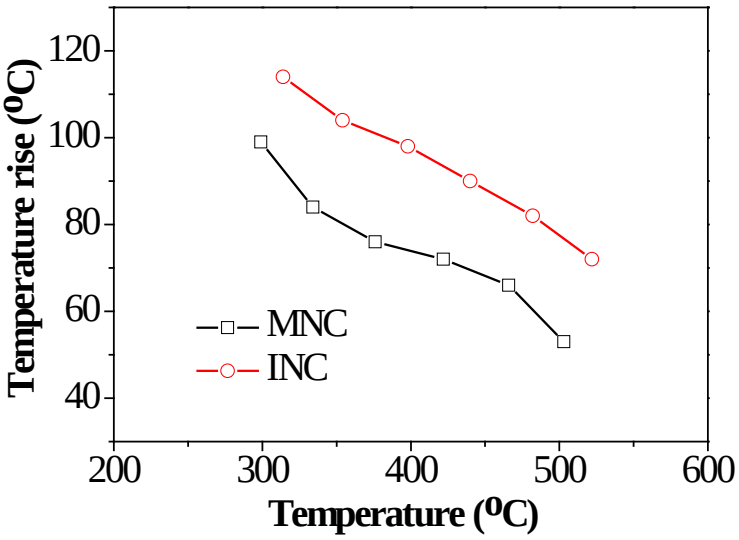

Figure 5

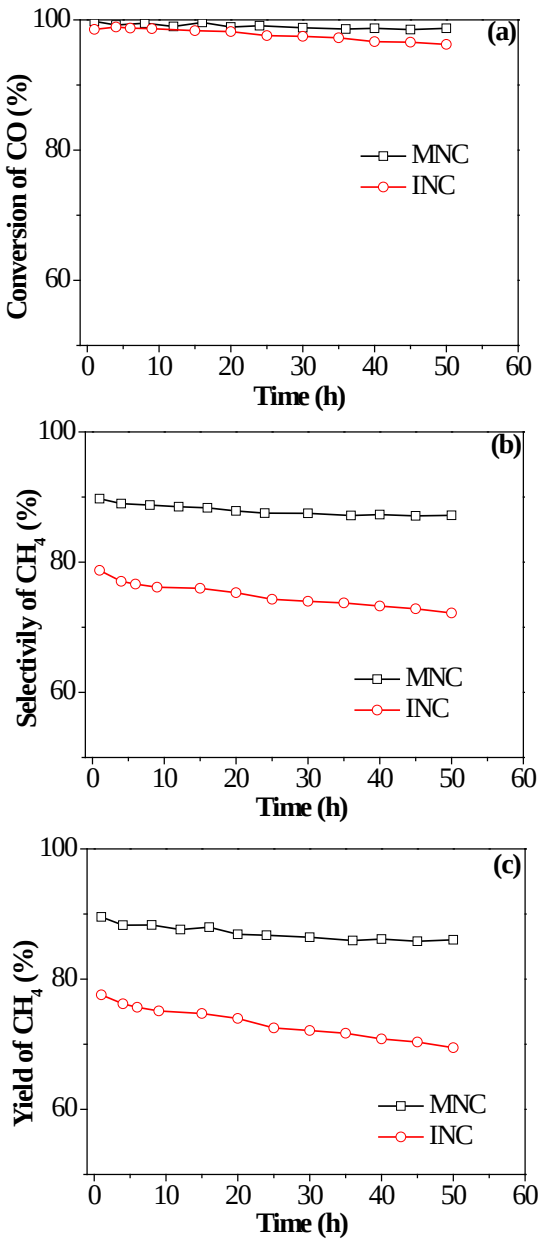

Figure 6

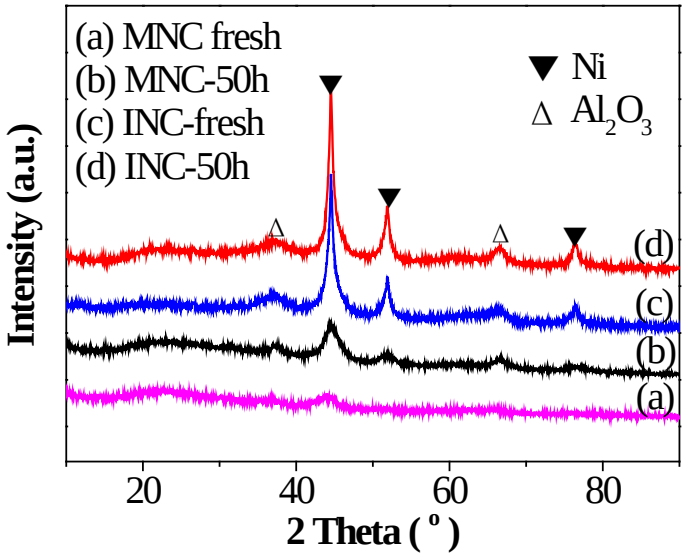

Figure 7

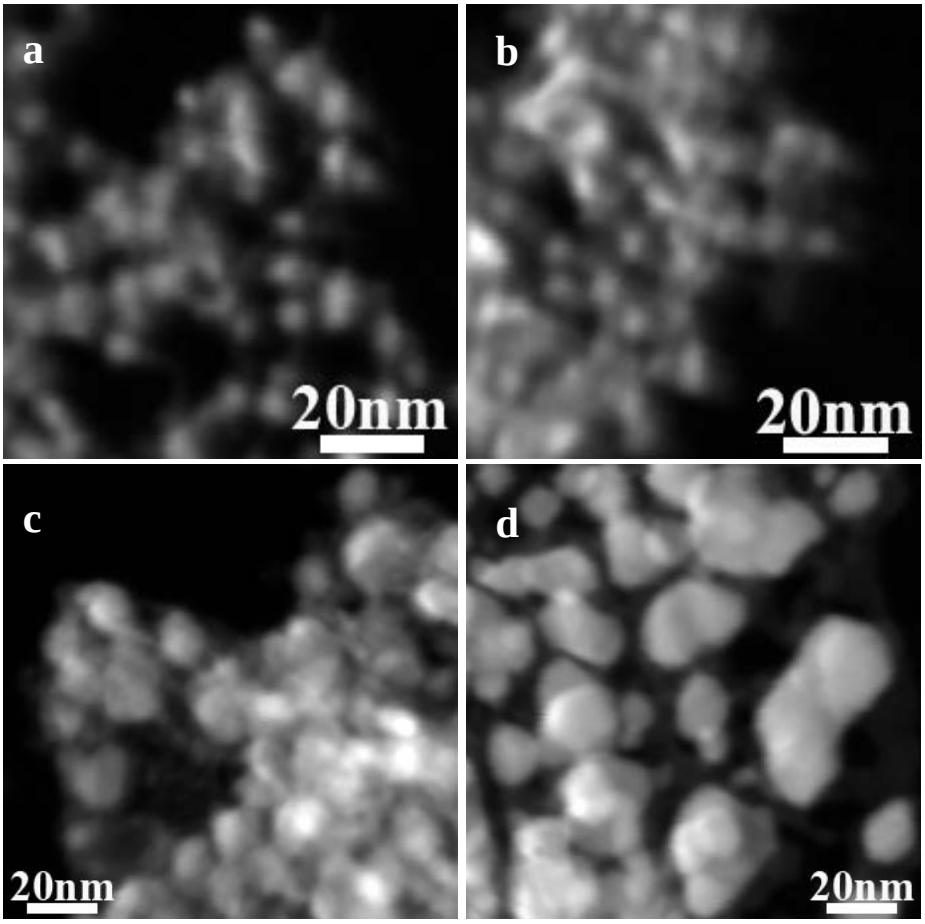

Figure 8

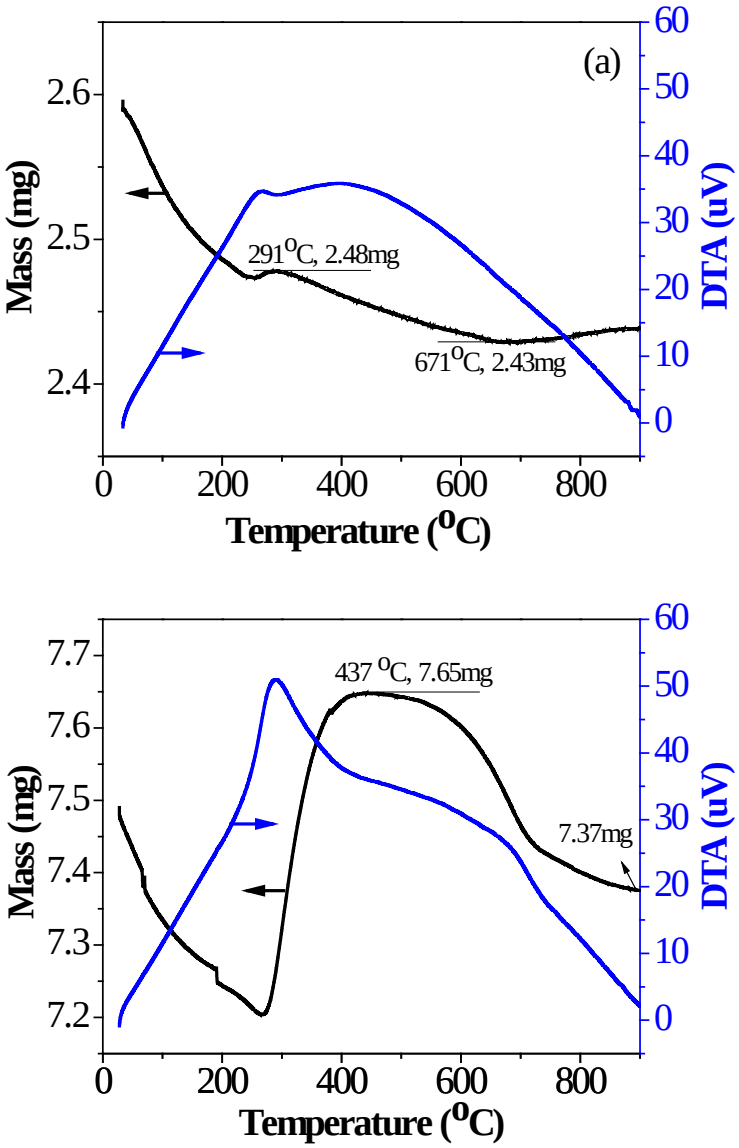

Figure 9

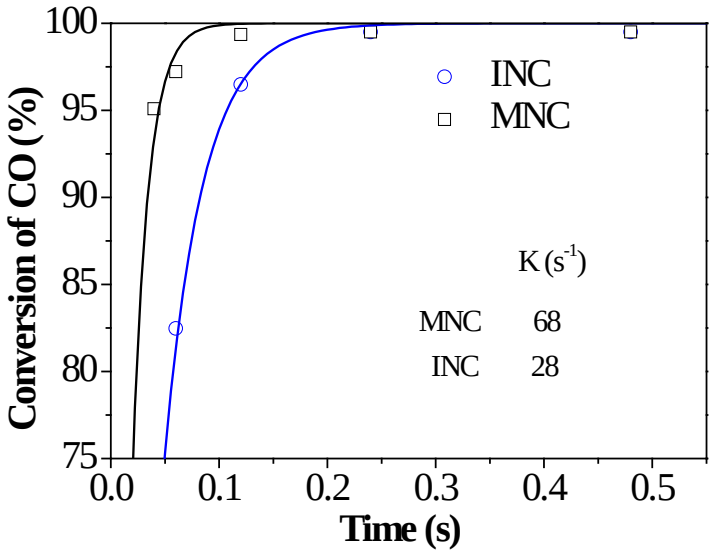

Figure 10

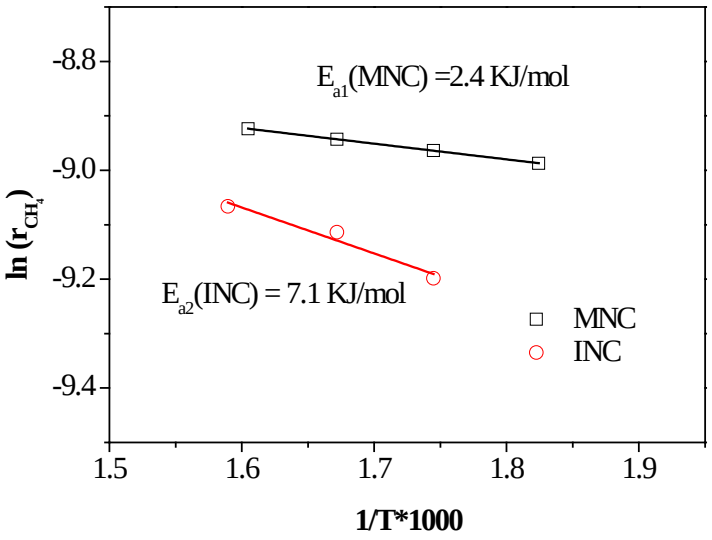

Figure 11